Available online at www.sciencedirect.com

ScienceDirect

Ceramics International 36 (2010) 313–322

CERAMICS INTERNATIONAL

www.elsevier.com/locate/ceramint

F-substituted hydroxyapatite nanopowders: Thermal stability, sintering behaviour and mechanical properties

Alessandra Bianco [a], Ilaria Cacciotti [a,*], Mariangela Lombardi [b], Laura Montanaro [b], Edoardo Bemporad [c], Marco Sebastiani [c]

[a] *Department of Chemical Sciences and Technologies, INSTM Research Unit Tor Vergata, University of Rome Tor Vergata, via Ricerca Scientifica, 00133 Rome, Italy*

[b] *Politecnico di Torino, Department of Materials Science and Chemical Engineering, INSTM Research Unit Politecnico di Torino: LINCE Lab, Torino, Italy*

[c] *Mechanical and Industrial Engineering Department, University of Rome 'Roma Tre', Via della Vasca Navale, 79-00146 Rome, Italy*

Received 8 July 2009; received in revised form 18 July 2009; accepted 10 August 2009
Available online 22 September 2009

Abstract

Fluorine-substituted hydroxyapatites are considered promising materials for bone scaffolding. In this study a systematic investigation on F-half substituted hydroxyapatite (F-HAp, $Ca_{10}(PO_4)_6OHF$) obtained by precipitation is reported. Results on composition analysis, thermal behaviour, and sinterability are presented for a comparison with the respective pure hydroxyapatite. Samples were characterised by electron microscopy, induced coupled plasma-atomic emission spectroscopy, thermal analysis, infrared spectroscopy, N_2 adsorption measurements, X-ray diffraction and dilatometry. A semicrystalline F-substituted hydroxyapatite powder made up of needle-like nanoparticles was obtained. Notwithstanding that it was thermally stable up to 1300 °C, it was sintered at relatively low temperatures obtaining a very fine microstructure with a relevant nanoporosity, beneficial in view of cell adhesion and in-growth.

Hardness, elastic modulus and toughness of produced samples were investigated by Vickers–Knoop microhardness testing. Significant improvements of the mechanical properties were observed for the F-substituted hydroxyapatite, in comparison with pure hydroxyapatite.

Keywords: A. Sintering; B. Electron microscopy; C. Mechanical properties; D. Apatite; E. Biomedical applications

1. Introduction

Synthetic hydroxyapatite (HAp, $Ca_{10}(PO_4)_6(OH)_2$) is widely used in dental, periodontal, oral/maxillofacial surgical procedures and skeletal bone surgery. However, the bioresorption of HAp under physiological conditions might affect implant reliability and lifetime, leading ultimately to failure. Fluorine-substituted hydroxyapatite (F-HAp, $Ca_{10}(PO_4)_6(OH,F)_2$) is considered as alternative potential candidate for bone repair due to its low solubility, good biocompatibility, high thermal and chemical stability [1]. It has been recently reported that F^- ions might stimulate extracellular matrix formation *in vitro* and enhance bone union *in vivo*, promoting osteoblastic activities in terms of cell proliferation and differentiation [2]. Besides F-HAps promote new mineralization of incipient lesions, prevent, reduce and control dental caries [3]. However, two serious health problems have been associated with high concentrations of fluoride in groundwater: dental and bone fluorosis which can evolve into a more severe illness such as osteosclerosis or exostosis [4,5]. Thus, it is necessary to tailor the F^- content in F-HAp so as to optimize the bioactivity of the implants in order to control the amount of fluoride ions released from F-HAp, because the higher the level of fluoridation, the more fluoride ions released [6]. The higher stability of F-HAp in biological environments with respect to HAp can also be considered as a positive factor for a prospective application, e.g. in bone drug delivery systems. In particular, it has been demonstrated that F-HAp implants showed good integration in the bone tissue and much longer resorption time than conventional calcium phosphates [7].

Many papers [1–7] analyse the influence of F incorporation within apatite lattice on the physicochemical properties of hydroxyapatite, such as crystallinity, thermal stability, solubility, and corrosion resistance, but a certain lack exists in

---

* Corresponding author. Tel.: +39 0672594482; fax: +39 0672594328.
E-mail address: ilaria.cacciotti@uniroma2.it (I. Cacciotti).

0272-8842/$36.00 © 2009 Elsevier Ltd and Techna Group S.r.l. All rights reserved.
doi:10.1016/j.ceramint.2009.09.007

literature among powder features, sinterability, final microstructure and mechanical behaviour of F-HAps.

The knowledge of mechanical properties is useful and fundamental for implant manufacturing. Load bearing applications require information on the fracture toughness, coupled to hardness for wear resistance [8], and to elastic modulus to determine the degree of stress shielding. Significant work has been already carried out on the mechanical properties of hydroxyapatite [9,10], while there is a lack of comprehensive mechanical property data for chemically modified apatites [11–13].

The objective of this paper is to compare a pure and a F-substituted hydroxyapatite materials, covering the overall ceramic process from the synthesis of the nanopowder to the sintered bodies characterisation. For this purpose, pure and F-half substituted hydroxyapatite nanopowders were synthesised by precipitation starting from $Ca(NO_3)_2{\cdot}6H_2O$, $(NH_4)_2HPO_4$ and NH_4F. Particle size and morphology were studied by Transmission Electron Microscopy (TEM), and specific surface area (SSA) measured by N_2 adsorption isotherms. Characteristic functional groups were evidenced by Fourier Transform Infrared Spectroscopy (FT-IR), the thermal behaviour displayed by thermal analysis (TG-DTA) and the thermal stability investigated by X-ray diffractometry (XRD and HT-XRD). Crystallinity degree, average crystallite size and cell parameters of *as-dried* samples were also calculated. The sintering behaviour was evaluated by thermal dilatometry. Results on density, microstructure and mechanical properties (elastic modulus, Vickers–Knoop microhardness, and fracture toughness) of sintered ceramics are finally presented and discussed.

2. Experimental details

2.1. Precipitation

Pure and F-substituted hydroxyapatite powders were synthesised in a double-walled jacket reactor at 40 °C under magnetic stirring, starting from calcium nitrate and diammonium hydrogen phosphate. Pure hydroxyapatite powder (HAp) was prepared adding drop-wise (3–4 drops/s) 250 ml of an 1 M aqueous solution of calcium nitrate tetrahydrate ($Ca(NO_3)_2{\cdot}4H_2O$, *Aldrich* 99.2%, MW 236.15) to a diammonium hydrogen phosphate ($(NH_4)_2HPO_4$, *Aldrich* 99.2%, MW 132.06) solution.

The pH was continuously monitored and adjusted to 10 ± 0.1 by adding conc. NH_4OH. More details on this synthesis are reported elsewhere [14].

F-half substituted hydroxyapatite powder ($Ca_{10}(PO_4)_6FOH$) was prepared, assuming that F^- ions would substitute for the hydroxide site in the HAp lattice in order to obtain a nominal composition in terms of Ca/P ratio of 1.667 (Table 1).

Ammonium fluoride (NH_4F, *Sigma–Aldrich* 99.99%, MW 74.10) was added to the $(NH_4)_2HPO_4$ solution, the same procedure described above was then followed.

Both precipitates were aged in mother liquor at room temperature for 24 h, washed with an aqueous NH_4OH solution, vacuum filtered, and finally dried in oven at 60 °C (*as-dried* samples).

Table 1
Designation, nominal composition and ICP-AES results of *as-dried* pure and F-substituted hydroxyapatite powders.

Sample	Formula	Nominal Ca/P molar ratio	Actual Ca/P molar ratio	Nominal [F] (mg/l)	Actual [F] (mg/l)
HAp	$Ca_{10}(PO_4)_6(OH)_2$	1.667	1.658	–	–
F-HAp	$Ca_{10}(PO_4)_6FOH$	1.667	1.7153	0.9567	0.9143

Sample designation and nominal compositions of synthesised materials are summarised in Table 1.

2.2. Powder characterisation

Chemical analyses of precipitates were performed by induced coupled plasma-atomic emission spectroscopy (*AES-ICP*, *JobinYvon JV 24R*). Detection limits of ICP analysis were 0.2 ppb at 393.366 nm for Ca and 76 ppb at 214.914 nm for P.

Fluorine concentration measurement was conducted using F-selective electrode (Orion 94-09) in a total ionic strength adjustment buffer (TISAB). 0.2 g of each sample was dissolved in 10 ml of 1 M nitric acid and then diluted by 200 ml deionised water. The fluorine content was determined by mixing 10 ml of such solution and 10 ml of the buffer. Standard solutions made from NaF were used to calibrate the measurement in the same buffer solution.

The thermal behaviour of *as-dried* samples was investigated by simultaneous thermogravimetry and differential thermal analysis (*TG-DTA*, *Netzsch STA 409*) in the following conditions: sample weight about 60 mg, heating rate 10 °C/min, peak temperature 1500 °C.

Microstructural features of *as-dried* powders were studied by Transmission Electron Microscopy (*TEM*, *Philips CM120*) in bright field mode, the accelerating voltage being 100 kV.

Infrared spectra (Fourier Transform Infrared Spectroscopy, *FT-IR PerkinElmer*) were recorded in the region 500–4000 cm^{-1} using KBr pellets (1%wt/wt), spectral resolution 4 cm^{-1}.

The specific surface area (SSA) of *as-dried* samples and powders heated at 600 °C was evaluated by N_2 adsorption (*Sorptomatic 1900*, *Carlo Erba Instruments*) using Brunauer–Emmett–Teller (BET) method. The specific surface area is then calculated from the volume of gas adsorbed in a monolayer [15].

The particle size (D_{BET}) was also estimated by assuming the primary particles to be spherical

$$D_{BET} = \frac{6}{\rho s}$$

where ρ is the theoretical density of the sample (3.156 g/cm^3 for HAp and 3.13 g/cm^3 for F-HAp) and s is the SSA [16].

X-ray diffraction (XRD) (*Philips X'Pert 1710*) (Cu Kα radiation λ = 1.5405600 Å, 20–55° 2θ, step size 0.010°, time per step 2 s, scan speed 0.005°/s) analyses were performed on both *as-dried* and calcined powders at different temperatures up to 1400 °C. Phase evolution of *as-dried* powders was followed by high-temperature XRD measurements (HT-XRD) (*Anton Paar HTK 1200*) in the following conditions: Cu Kα radiation λ = 1.5405600 Å, 20–55° 2θ, heating rate 5 °C/min, peak temperature 1100 °C, step size 0.010°, time per step 2 s, scan speed 0.005°/s.

According to Ref. [17], the crystallinity degree of *as-dried* samples (X_c), corresponding to the fraction of crystalline phase present in the examined volume, was evaluated as follows:

$$X_c \approx 1 - \frac{V_{112/300}}{I_{300}}$$

where I_{300} is the intensity of the (3 0 0) reflection of HAp and $V_{112/300}$ is the intensity of the hollow between the (1 1 2) and the (3 0 0) reflections, which completely disappears in non-crystalline samples. In agreement with Ref. [17], a verification was made as follows:

$$B_{002}\sqrt[3]{X_c} = K$$

where K is a constant equal to 0.24 for a very large number of different HAp powders, and B_{002} is the full width at half maximum (in degrees) of the (0 0 2) reflection.The average crystallite size $D_{(hkl)}$ in nm was estimated following the Debey–Scherrer equation [18]:

$$D_{(hkl)} = \frac{K\lambda}{\sqrt{\varpi^2 - \varpi_0^2}\cos\theta}$$

where K is the shape factor equal to 0.9, λ is the X-ray wavelength (i.e. 1.541 Å for Cu Kα radiation), θ is the Bragg's diffraction angle (in degrees) and ω is the full width at half maximum (FWHM). The diffraction peak at 25.8° (2θ) corresponding to the (0 0 2) Miller plane family of HAp (JCPDS files #09-0432), and the diffraction peak at 32.9° (2θ) corresponding to the (3 0 0) Miller plane family, were chosen to calculate the average crystal size along to the crystallographic axis c and a, respectively, ω_0 corresponds to the instrumental width [19]. Cell parameters of pure and substituted HAps were estimated through the algorithm *TREOR* (*Philips X'Pert Plus software*).

2.3. Sintering behaviour

On the grounds of TG-DTA and XRD analyses, powders were pre-treated at 600 °C for 1 h (heating and cooling rate of 10 °C/min) to prevent relevant weight losses during the densification process. Bars were cold uniaxially pressed at 400 MPa and dilatometric analyses (*Netzsch 402E*) were performed in the following conditions: peak temperature 1250 °C, soaking time 1 h, heating and cooling rate 10 °C/min. On the grounds of the resulting shrinkage, sintering cycles at a lower maximum temperature were also performed. Green densities were calculated by geometrical and mass measurements, whereas fired density values evaluated by Archimede's method. Final microstructures were observed on fracture surfaces by Scanning Electron Microscope (*SEM, Hitachi S 2300*).

2.4. Mechanical characterisation of samples

The 600 °C-treated powders were uniaxially pressed at about 120 MPa in a 12 mm diameter cylindrical die. Green bodies were sintered in air in the following conditions: peak temperature 1250 °C, soaking time 1 h, heating and cooling rate 10 °C/min.

Knoop microhardness testing was adopted for the evaluation of the elastic modulus of produced samples; five indentations were performed on each sample at an applied load of 1 N (which was enough to have easily readable indentation marks by optical microscopy, also avoid cracking of samples — test parameters according to the standard ASTM E384-99 [20]).

The elastic modulus (E) was then calculated according to the procedure described in Ref. [21], being:

$$\frac{H_K}{E} = \frac{0.14 - (b/d)}{0.45}$$

where b and d are the lengths of the shorter and longer Knoop diagonals, respectively.

Hardness and Indentation Size Effect (ISE) curve were investigated by Vickers indentation testing and hardness modelling, applied load ranging from 50 down to 5 gf (also in this case, test parameters according to the standard ASTM E384-99). Five indentations were carried out for each load.

The Indentation Size Effect (ISE) Meyer's law [22] was finally adopted to describe the relation between load and size of indentation:

$$P = kd^n$$

where P is the applied load, d is the indentation size, k and n are constants.

The above equation can be rewritten as a function of Vickers hardness:

$$H_V = H_{V0}d^{n-2}$$

Coefficient n is known as Meyer's or hardening index, generally slightly lower than 2.0 for pyramidal indenters [22], while H_{V0} is a constant. If n is equal to 2.0, there is no ISE in the analysed sample.

Vickers hardness testing was also adopted for fracture toughness evaluation of the analysed samples: during sharp indentation of brittle materials, radial cracks can be generated during unloading due to the residual crack opening force given by the plastic deformed zone under the indenter [23].

Under sharp indenters, two distinct types of crack are found in planes perpendicular to the direction of indentation: (1) radial median crack type, where the crack is generated all under the indent, and (2) Palmqvist crack type, where a crack is developed only at the corners of the indent [23].

The Vickers indentation of brittle calcium phosphate materials causes the creation of crack patterns that can be described mainly according to the radial median crack system. This assumption has been confirmed when analysing the relationship between crack length, 2c, and load, P, as well as using the c/a ratio analysis for a chosen load.

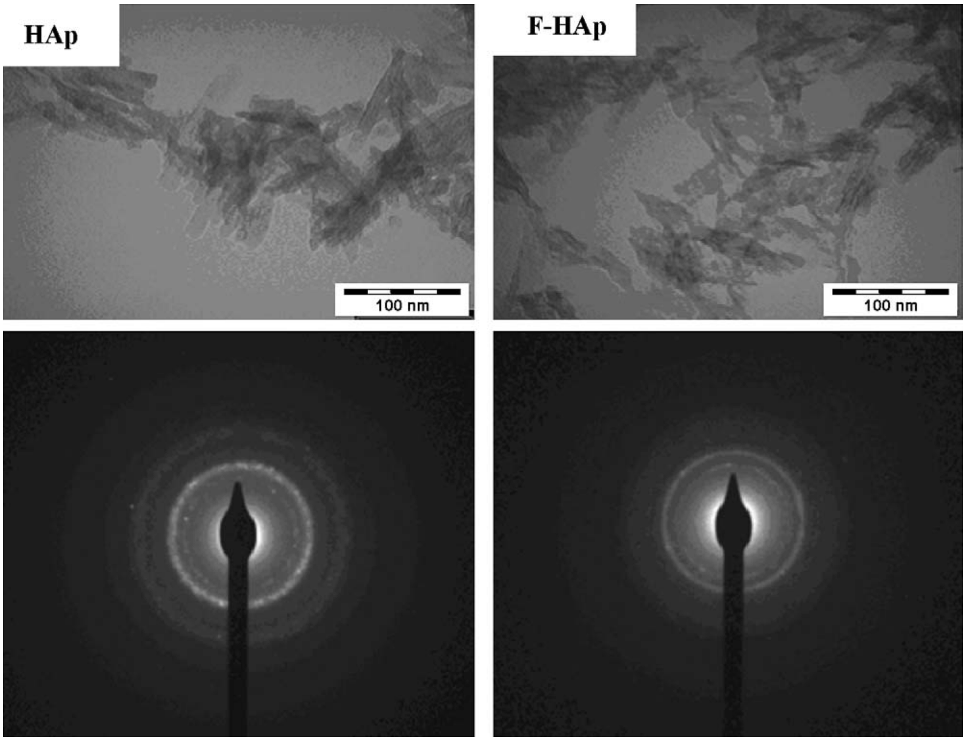

Fig. 1. TEM images and selected area electron diffraction (SAED) patterns of *as-dried* HAp and F-HAp nanopowders (magnification 300,000×).

Fracture toughness (K_C) can be therefore calculated as follows, by the use of the well known model developed by Lawn et al. [23], based on a radial median crack type assumption:

$$K_C = 0.028(H_V a^{1/2})\left(\frac{E}{H_V}\right)^{1/2}\left(\frac{c}{a}\right)^{-1.5}$$

where a and c are the half diagonals of the Vickers indent and of the crack, respectively.

The data on the crack length was taken from Vickers indentations at an applied load of 20 N.

Finally, the brittleness index has been determined by the following equation [24]:

$$B = \frac{H}{K_C}$$

3. Results and discussion

3.1. Composition, microstructure and thermogravimetry

The results of ICP-AES analyses of *as-dried* powders are reported in Table 1. It is evidenced that the Ca/P atomic ratio of pure hydroxyapatite was close to the stoichiometric value of 1.667. In the case of F-HAp, the actual Ca/P molar ratio was higher than the nominal one, probably due to P loss. Moreover, the measured fluorine content was close to the nominal value (Table 1).

Particle size and morphology of *as-dried* powders were determined by TEM observations. It resulted that samples are composed of nano-sized, needle-like particles 10–20 nm wide and 50–200 nm long. TEM micrographs and the correspondent selected area electron diffraction (SAED) patterns of samples HAp and F-HAp are presented in Fig. 1. The incorporation of fluoride within the apatite lattice does not seem to significantly affect the size and morphology of nanoparticles [25–27]. The SAED patterns exhibit spotted sharp and continuous rings that evidence polycrystalline grains.

TG curves of all *as-dried* precipitates showed 3–5% weight losses in the range 150–600 °C, due to the removal of combined water and carbonates, in good agreement with literature data [28,29].

XRD patterns of *as-dried* pure and F-substituted hydroxyapatite powders are compared in Fig. 2. Both spectra showed only reflections associated to HAp according to JCPDS

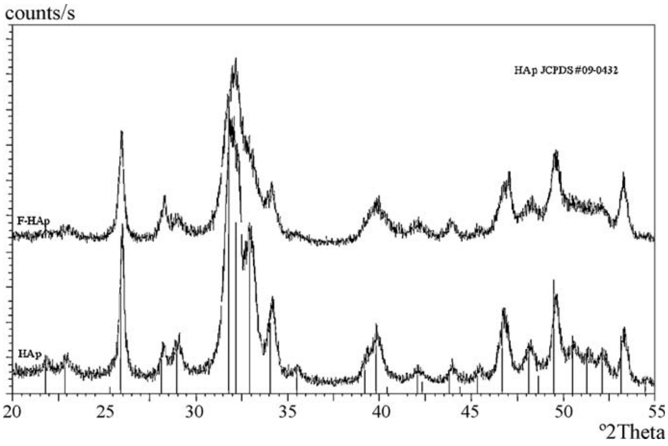

Fig. 2. XRD patterns of *as-dried* HAp and F-HAp nanopowders.

#09-0432. The estimated crystallinity degree was around 60% and 40% for HAp and F-HAp, respectively.

The mean crystallite size of *as-dried* HAp sample was about 40 nm and about 20 nm, along *c*-axis and *a*-axis, respectively. In the case of F-HAp, the mean crystallite size was about 116 nm and 36 nm, along *c*-axis and *a*-axis, respectively. In good agreement with the literature an increased crystallite size, especially along the *c*-axis direction, was observed [30,31].

3.2. Thermal stability

In Fig. 3a high-temperature XRD (HT-XRD) analyses of the pure hydroxyapatite powder are presented. They were performed in order to better assess the decomposition temperature. HAp was thermally stable up to 960 °C; above this temperature the α-TCP metastable phase appeared [JCPDS #70-0364]. On the other side, in Fig. 3b the XRD spectra of substituted sample calcined at different temperatures are reported. F-HAp was thermally stable up to about 1300 °C, while at higher temperatures α-TCP phase appeared. The increased stability of F-HAp could be explained considering that a more ordered apatite structure is formed. In details, in the HAp lattice the hydrogen atoms of the OH group are randomly arranged in atomic interstices neighbouring to the oxygen atoms, conferring a certain disorder to the crystal structure. In the case of F-HAp, the hydrogen atoms of the hydroxyl groups are tightly bound to the nearby F^- anions, producing a well-ordered apatite structure [27].

Table 2
Calculated cell parameters of pure and F-substituted hydroxyapatite powders.

Sample	*a* (Å)	*b* (Å)	*c* (Å)	$V/10^6$ (pm^3)
HAp	9.422(3)	9.422(3)	6.884(2)	529.201
F-HAp	9.39(1)	9.39(1)	6.882(9)	525.992

Lattice parameters are reported in Table 2, the reference for hydroxyapatite being JCPDS #09-0432 ($a = b = 9.418$ Å, $c = 6.884$ Å, space group P63/m, theoretical density 3.156 g/cm^3, $Z = 1$). In agreement with the literature [27,31], a slight decrement of lattice constants was detected. The value of the calculated *a*-axis of F-half substituted HAp was between that of HAp and that of fluoroapatite ($Ca_{10}(PO_4)_6F_2$) according to JCPDS #15-0876 ($a = 9.364$ Å) [25,31], due to the smaller size of F^- (1.32 Å) with respect to OH^- (1.68 Å) [1,11,27,32]. On the other side, the lattice parameter *c* does not significantly change [25].

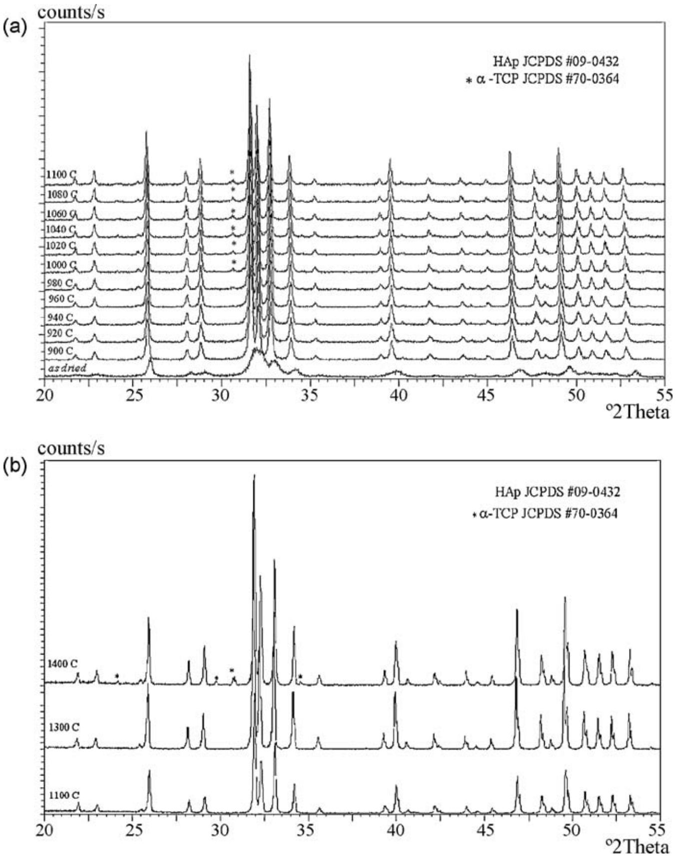

Fig. 3. (a) HT-XRD spectra of sample HAp recorded between 30 °C and 1100 °C, (b) XRD spectra of F-HAp powder calcined at 1100 °C, 1300 °C and 1400 °C.

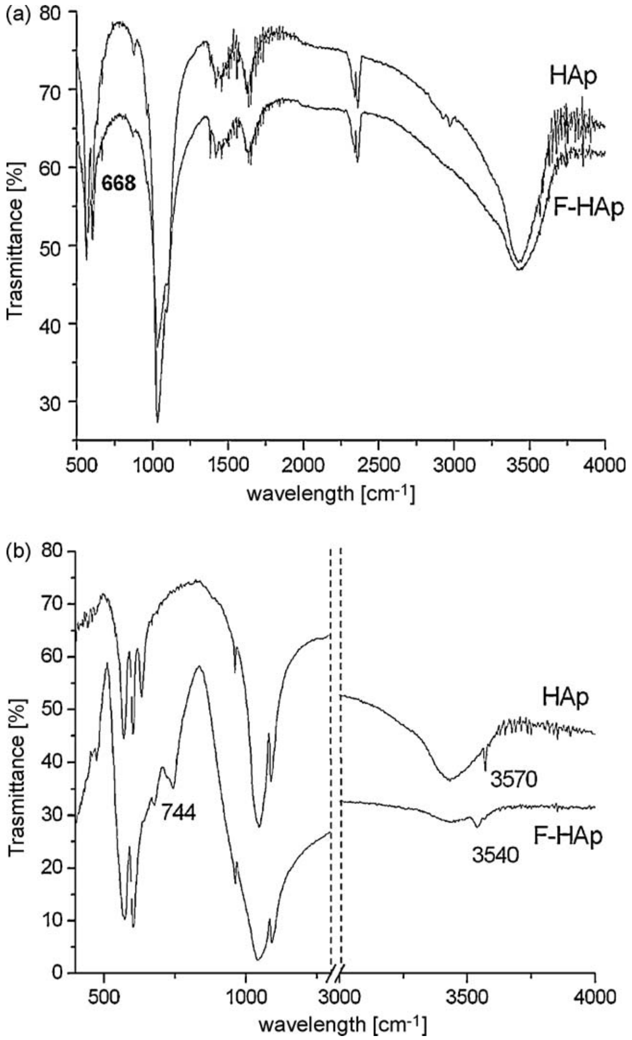

Fig. 4. (a) FT-IR spectra of *as-dried* HAp and F-HAp powders, (b) FT-IR spectra of 1100 °C-calcined HAp and F-HAp powders.

Table 3
Specific surface area (SSA) and average particle size (D_{BET}) of pure and F-substituted hydroxyapatite powders.

Sample	SSA (m^2/g)		D_{BET}[a] (nm)
	As-dried[b]	Calcined at 600 °C	
HAp	77	45	25
F-HAp	118	45	16

[a] The average particle size (D_{BET}) was calculated on *as-dried* sample.
[b] Samples were preliminarily treated with EtOH in order to eliminate absorbed water.

3.3. FT-IR analysis of pure and F-substituted hydroxyapatites

In Fig. 4a and b the FT-IR spectra of *as-dried* and 1100 °C-treated samples are reported.

The patterns of *as-dried* samples (Fig. 4a) show the characteristic pattern of partially carbonated hydrated HAps as extensively discussed elsewhere [14]. In particular, bands at 3570 and 631 cm^{-1}, corresponding to the stretching and vibrational mode of the OH^- groups, respectively, were evidenced for HAp. As expected, the spectrum of F-HAp did not show these peaks [33]. The vibrational bands of phosphate were observed in all the samples, at 602 and 566 cm^{-1}. Moreover, in the case of F-HAp sample, an extra peak was recorded at 668 cm^{-1}; associable to the "tail to tail" configuration $\cdots$HO:OH$\cdots$ in an OH chain of variable length [34]. FT-IR of calcined samples (Fig. 4b) differed considerably from *as-dried* materials. In details, in the case of HAp sample, all bands associated to carbonate ions disappeared, bands associated to combined water at 1636 and 3430 cm^{-1} decreased, and intensity of OH^- vibration mode at 3570 cm^{-1} remarkably increased. In the case of F-HAp sample, peak ascribed to OH^- vibration mode at 3570 cm^{-1} was shifted to 3540 cm^{-1}, but this band could be associated to OH^- bonded directly to F^- in the configuration OHF^- [34]. Furthermore, in the case of F-HAp an extra peak at 744 cm^{-1} was observed and it could be ascribed to the configuration

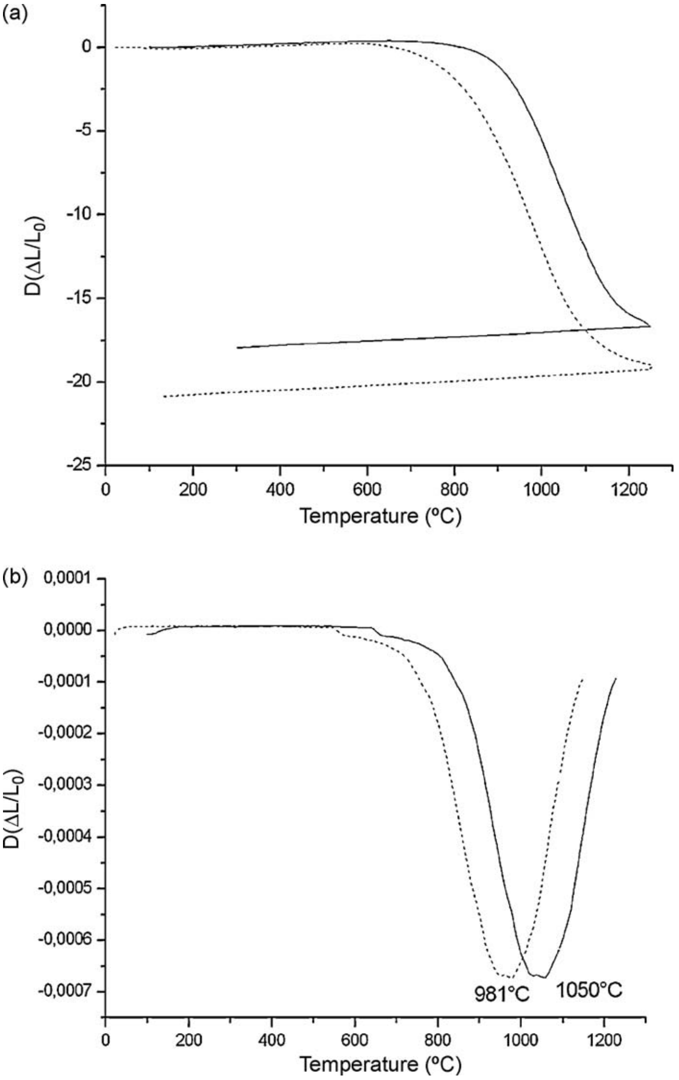

Fig. 6. (a) Dilatometric curves of pure (*solid line*) and F-substituted (*dotted line*) hydroxyapatite powders, (b) derivative curves of pure (*solid line*) and F-substituted (*dotted line*) hydroxyapatite powders.

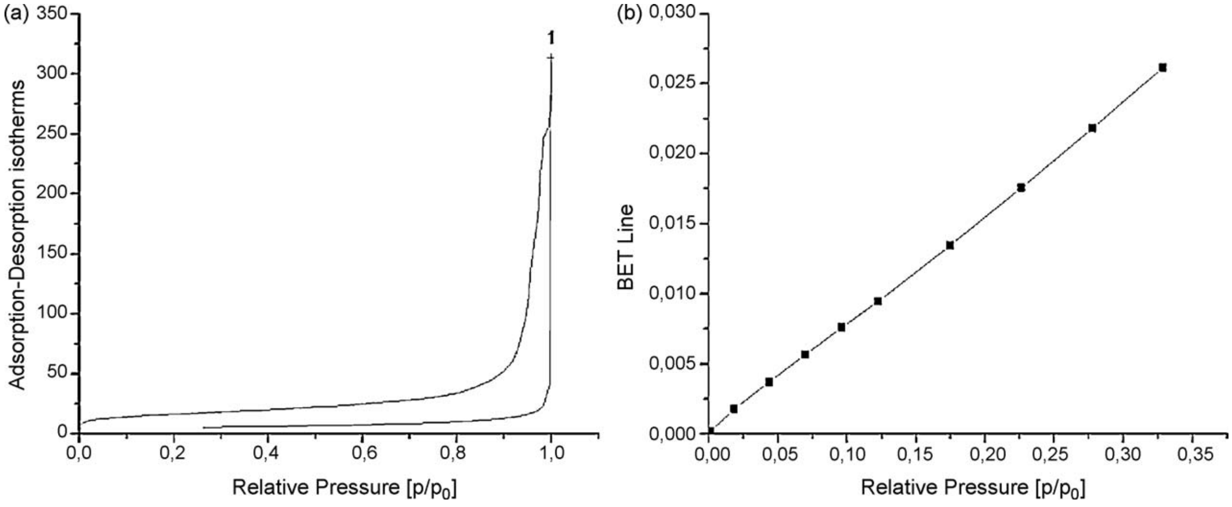

Fig. 5. (a) Adsorption–desorption isotherms of *as-dried* F-HAp nanopowder, (b) BET lines of *as-dried* F-HAp nanopowder.

FFOHFF, in which the single OH^- group could be between two orientations, ···FOHF··· or ···FHOF··· and may switch from the one to the other with a comparatively low energy [34]. A correlation between the gradual introduction of fluoride in HAp and the increase of intensity of a band around 720–740 cm^{-1} accompanied by the decrease of intensity of the 630 cm^{-1} band was described [34].

3.4. Specific surface area of pure and F-substituted hydroxyapatites

The specific surface area (SSA) of *as-dried* and calcined powders has been determined by N_2 absorption isotherms: results are presented in Table 3. It resulted that F-HAp showed a much higher SSA with respect to the corresponding pure HAp, in good agreement with Ref. [35]. In Fig. 5a the adsorption–desorption curves of *as-dried* F-HAp are shown.

In Fig. 5b the corresponding BET line is reported, the high correlation factor (0.999) giving evidence for the accuracy of SSA measurements. As expected, the SSA of 600 °C-calcined nanopowders were much lower with respect to *as-dried* samples, no significant difference was evidenced among samples. Moreover, the average particle size (D_{BET}), calculated on *as-dried* powders, was for both samples about 20 nm.

3.5. Sintering behaviour of pure and F-substituted hydroxyapatites

The dilatometric and derivative curves are compared in Fig. 6a and b, up to a sintering temperature of 1250 °C. Pure HAp showed a shrinkage onset temperature around 800 °C, the maximum sintering rate temperature being located at about 1040 °C. The shrinkage was almost completed during the heating step and reached a total value of about 18%. On the contrary, F-substituted HAp was characterised by a displacement of the characteristic sintering temperatures to lower values. In fact, the onset temperature was decreased to about 600 °C and the maximum shrinkage rate temperature displaced to about 981 °C. Also in the case of the F-HAp nanopowder, the overall shrinkage was almost completed within the heating step, reaching a final value of 21%. Green and fired densities (expressed as percentage with respect to the theoretical values

Table 4
Density and sintering data of pure and F-substituted hydroxyapatite materials.

Sample	Linear shrinkage (%)	Onset temperature (°C)	Green density (g/cm^3)	Fired density 1250 °C/1 h (g/cm^3)	Fired density 1100 °C/3 h (g/cm^3)
HAp	18.2	1040	1.68 [53%TD]	3.07 [97%TD]	–
F-HAp	20.8	981	1.60 [51%TD]	3.13 [100%TD]	3.01 [96%TD]

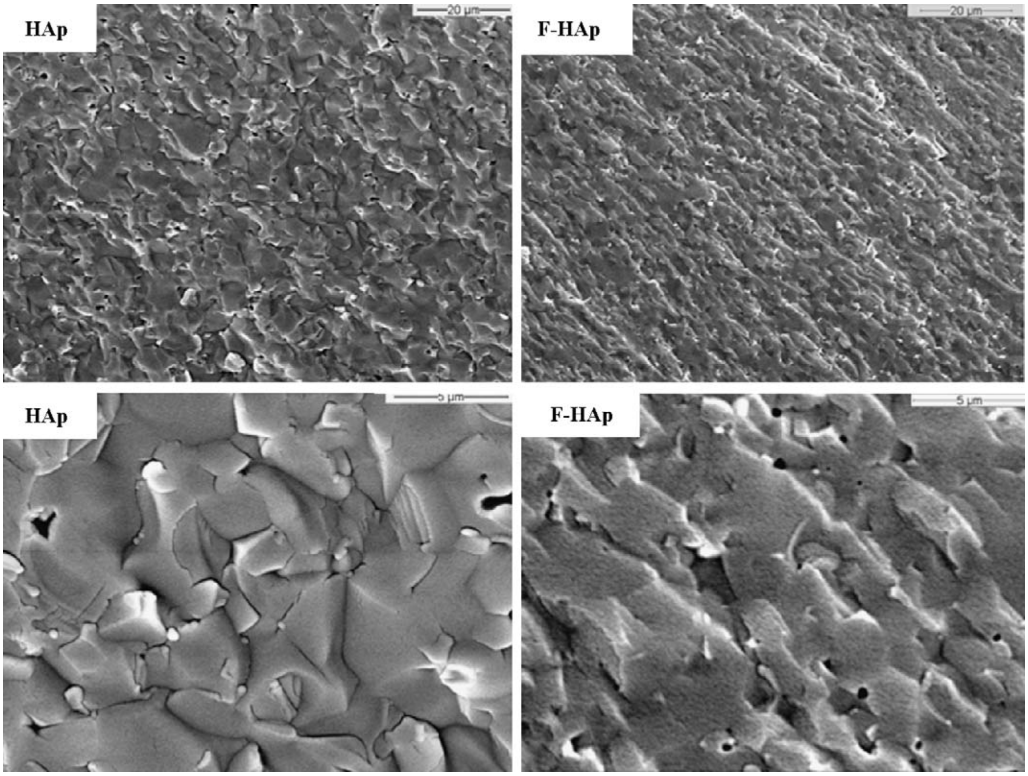

Fig. 7. SEM micrographs of fracture surfaces of pure and F-substituted hydroxyapatite materials sintered at 1250 °C for 1 h.

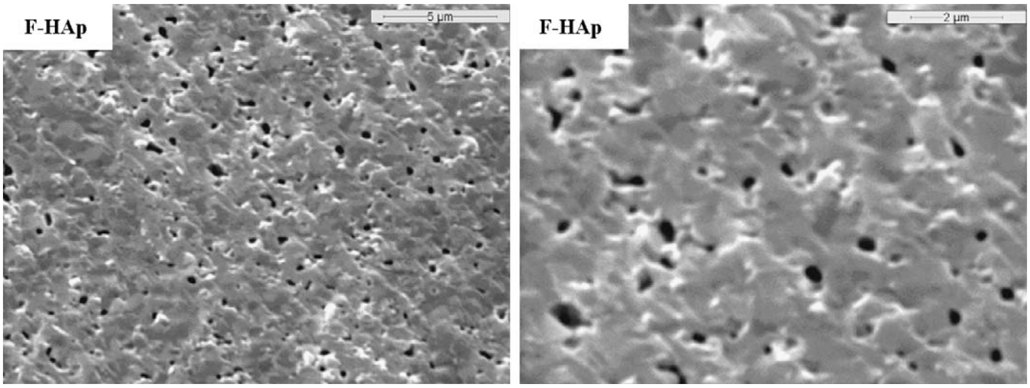

Fig. 8. SEM micrographs of fracture surfaces of F-substituted hydroxyapatite material sintered at 1100 °C for 3 h.

(TD = theoretical density) equal to 3.16 and 3.13 g/cm^3 for pure and F-substituted HAp, respectively) are collected in Table 4. It should be pointed out that, on the basis of XRD results, at the sintering temperature F-HAp sample was single-phase hydroxyapatite, while pure HAp presented also α-TCP as second phase. Thus, in the last case, fired density values, expressed as percentage of the theoretical value, were partially affected by the presence of α-TCP.

SEM images of the materials sintered at 1250 °C for 1 h are compared in Fig. 7: pure HAp powder presented a relevant grain growth and coalescence, with some residual pores located mainly at the triple joints. On the other hand, F-substituted ceramic showed a limited final porosity. On the basis of previous densification tests, new sintering cycles were set-up for F-HAp sample, which was sintered at 1100 °C for 3 h. A lower density value was reached, due to a more relevant residual porosity. However, the low-temperature-fired material does not undergo grain growth and coalescence phenomena, as shown in Fig. 8.

3.6. Mechanical properties of pure and F-substituted sintered hydroxyapatites

Results of Vickers hardness testing are presented in Table 5. The ISE curve for both pure HAp and F-HAp are reported in Fig. 9. It can be observed how the incorporation of F mainly involved a significant increase of fracture toughness of the samples, with a consequent decrease of the brittleness index (H/K_C).

This behaviour suggests that the addition of vicarious ions can play a significant role in crack propagation mode and fracture toughness of substituted HAp, likely due to a different densification behaviour.

Table 5
Microhardness (H_{V0}, n – Meyer ISE model), fracture toughness (K_C), brittleness index (H/K_{IC}) and Young modulus (E) of pure and F-substituted hydroxyapatite materials, as measured by microindentation testing.

Sample	H_{V0} [GPa] (Meyer)	n (Meyer)	K_C [MPa m$^{-0.5}$]	B [µm-0, 5]	E [GPa]
HAp	8.64	1.827	0.92	9.39	121.46
F-HAp	8.74	1.923	1.15	7.6	128.94

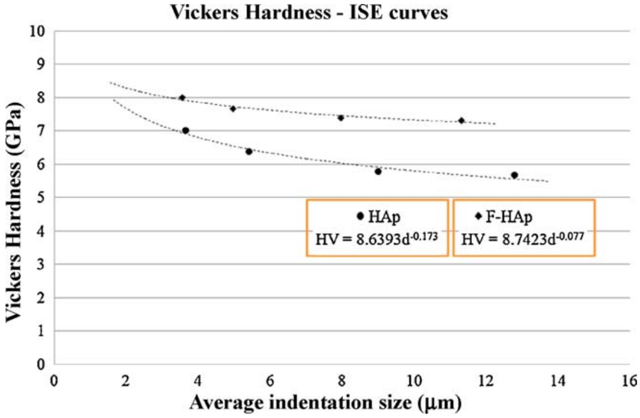

Fig. 9. Indentation Size Effect (ISE) curves (Meyer model) for pure (circles) and F-substituted (squares) hydroxyapatite samples.

Moreover, a slight increase of elastic modulus and hardness values was observed, being measured data in good agreement with Ref. [13].

However, the obtained ISE curves clearly showed that higher Vickers hardness was obtained at all applied loads in the case of F-HAp sample (Fig. 9).

The pure HAp presented a higher hardening coefficient n (Meyer ISE model); this effect could be due to differences in both surface roughness and grain size between pure and F-substituted HAps. Furthermore, this result agrees with Ref. [36], being generally lower n values associated with higher H_{V0} data for polycrystalline ceramics.

The measured elastic modulus and hardness values also indicated that high density samples were obtained.

It is worth noting that the specifically developed mechanical characterisation procedure, completely based on indentation testing, leads to a correct and straightforward determination of the existing correlations between process parameters and mechanical properties of samples.

The observed reproducibility of experimental data also confirmed that by the combined use of Vickers–Knoop microindentation techniques, and a proper application of the models available in literature, reliable data can be obtained on elastic modulus, hardness and fracture toughness of samples; indentation testing is then confirmed to be an effective microprobe for the investigation of mechanical properties of dense ceramic bodies.

4. Conclusions

The synthesis of pure and F-half substituted hydroxyapatite nanopowders was successfully pursued starting from $Ca(NO_3)_2{\cdot}4H_2O$, $(NH_4)_2HPO_4$, and NH_4F. This process allowed a strict control over the chemical composition of hydroxyapatite nanopowder. Pure HAp decomposed around 1000 °C, resulting in a biphasic calcium phosphate material (BCP). Concerning F-HAp, the presence of F within the apatite lattice induced higher thermal stability, the decomposition occurring above 1300 °C. Dense (>90%) sintered ceramics were obtained by sintering at 1250 °C.

A displacement of the characteristic sintering temperatures (i.e. the onset temperature as well as the maximum densification rate temperature) was observed with the introduction of the F ions in the apatite lattice. Moreover, the F-HAp powder allows a low-temperature sintering, limiting grain growth and coalescence phenomena.

A specifically developed procedure based on microindentation testing was applied for elastic modulus, hardness and fracture toughness evaluation of procedure samples. Hardness characterisation results indicated that high density samples were obtained in both cases and that a significant increase of fracture toughness was observed for F-half substituted HAp compared to pure one.

Acknowledgments

This work was supported by PRIN 2006–2008 project titled ‘‘Design and realization of organic, inorganic and hybrid nanostructured scaffolds as substrates for the differentiation of stem cells in regenerative medicine’’.

The authors wish to acknowledge Dr. C. Bellitto and Dr. E. Bauer, ISM, CNR-Montelibretti, Rome-Italy, for FT-IR facilities.

Mechanical characterisation activities were carried out at the Interdepartmental Laboratory of Electron Microscopy (LIME), University Roma Tre, Rome, Italy, http://www.lime.uniroma3.it.

References

[1] M. Okazaki, Y. Miake, H. Tohda, T. Yanagisawa, T. Matsumoto, J. Takahashi, Functionally graded fluoridated apatites, Biomaterials 20 (1999) 1421–1426.

[2] J. Harrison, A.J. Melville, J.S. Forsythe, B.C. Muddle, A.O. Trounson, K.A. Gross, Sintered hydroxyfluorapatites–IV: the effect of fluoride substitutions upon colonisation of hydroxyapatites by mouse embryonic stem cells, Biomaterials 25 (2004) 4977–4986.

[3] E. Bertoni, A. Bigi, G. Cojazzi, M. Gandolfi, S. Panzavolta, N. Roveri, Nanocrystals of magnesium and fluoride substituted hydroxyapatite, J. Inorg. Biochem. 72 (1998) 29–35.

[4] K.W. Lau, K. Kesson, C.R. Libanati, D.J. Baylink, Osteogenic actions of fluoride: its therapeutic use for established osteoporosis, in: J.F. Whitfield, P. Morley (Eds.), Anabolic Treatments for Osteoporosis, CRC Press, Boca Raton, FL, 1998, p. 207.

[5] V.E. Badillo-Almaraz, J. Armando Flores, H. Arriola, F.A. López, L. Ruiz-Ramirez, Elimination of fluoride ions in water for human consumption using hydroxyapatite as an adsorbent, J. Radioanal. Nucl. Chem. 271 (2007) 741–744.

[6] H. Qu, M. Wei, The effect of fluoride contents in fluoridated hydroxyapatite on osteoblast behaviour, Acta Biomater. 2 (2006) 113–119.

[7] V.S. Kornlev, S.M. Barinov, E. Girardin, S. Oscarsson, A. Rosengren, F. Rustichelli, V.P. Orlovskii, Porous spherical hydroxyapatite and fluorhydroxyapatite granules: processing and characterization, Sci. Technol. Adv. Mater. 4 (2003) 503–508.

[8] K.A. Gross, M. Babovic, Influence of abrasion on the surface characteristics of thermally sprayed hydroxyapatite coatings, Biomaterials 23 (2002) 4731–4737.

[9] M. Akao, H. Aoki, K. Kato, Mechanical properties of sintered hydroxyapatite for prosthetic application, J. Mater. Sci. 16 (1981) 809–812.

[10] W. Suchanek, M. Yoshimura, Processing and properties of hydroxyapatite-based biomaterials for use as hard tissue replacement implants, J. Biomed. Mater. Res. 13 (1998) 94–117.

[11] I. Manjubala, M. Sivakumar, S. Najma Nikkath, Synthesis and characterisation of hydroxy/fluoroapatite solid solution, J. Mater. Sci. 36 (2001) 5481–5486.

[12] M. Wei, J.H. Evans, Synthesis and characterisation of hydroxyapatite and fluorapatite, Key Eng. Mater. 218–222 (2002) 35–38.

[13] K.A. Gross, L.M. Rodrıguez-Lorenzo, Sintered hydroxyfluorapatites. Part II: mechanical properties of solid solutions determined by microindentation, Biomaterials 25 (2004) 1385–1394.

[14] A. Bianco, I. Cacciotti, M. Lombardi, L. Montanaro, G. Gusmano, Thermal stability and sintering behaviour of hydroxyapatite nanopowders, J. Therm. Anal. Calor. 88 (2007) 237–243.

[15] L. Clausen, I. Fabricius, BET measurements: outgassing of minerals, J. Colloid Interface Sci. 227 (2000) 7–15.

[16] F.B. Ayed, J. Bouaziz, K. Bouzouita, Calcination and sintering of fluorapatite under argon atmosphere, J. Alloy Compd. 322 (2001) 238–245.

[17] E. Landi, A. Tampieri, G. Celotti, S. Sprio, Densification behaviour and mechanisms of synthetic hydroxyapatites, J. Eur. Ceram. Soc. 20 (2000) 2377–2387.

[18] E. Bouyere, F. Gitzhofer, M.I. Boulos, Morphological study of hydroxyapatite nanocrystal suspension, J. Mater. Sci.: Mater. Med. 11 (2000) 523–531.

[19] A. Siddharthan, S.K. Seshadri, T.S. Sampath Kumar, Microwave accelerated synthesis of nanosized calcium deficient hydroxyapatite, J. Mater. Sci.: Mater. Med. 15 (2004) 1279–1284.

[20] ASTM E384-99 A, Standard Test Method for Microindentation Hardness of Materials, 1984.

[21] D.B. Marshall, T. Noma, A.G. Evans, A simple method for determining elastic-modulus to hardness ratios using Knoop indentation methods, J. Am. Ceram. Soc. 65 (1982) 175–176.

[22] D. Tabor, The Hardness of Metals, Clarendon Press, Oxford, 1951.

[23] B.R. Lawn, A.G. Evans, D.B. Marshall, Elastic/plastic indentation damage in ceramics: the median/radial crack system, J. Am. Ceram. Soc. 63 (1980) 574–581.

[24] B.R. Lawn, D.B. Marshall, Hardness, toughness and brittleness: an indentation approach, J. Am. Ceram. Soc. 62 (1979) 347–350.

[25] M. Wei, T. Bostrom, L. Grondahl, Synthesis and characterization of hydroxyapatite, fluoride-substituted hydroxyapatite and fluorapatite, J. Mater. Sci.: Mater. Med. 14 (2003) 311–320.

[26] L.J. Jha, S. Best, J.C. Knowles, I. Rehman, J.D. Santos, W. Bonfield, Preparation and characterization of fluoride-substituted apatites, J. Mater. Sci.: Mater. Med. 8 (1997) 185–191.

[27] Y. Chen, X. Miao, Thermal and chemical stability of fluorohydroxyapatite ceramics with different fluorine contents, Biomaterials 26 (2005) 1205–1210.

[28] Y.X. Pang, X. Bao, Influence of temperature, ripening time and calcination on the morphology and crystallinity of hydroxyapatite nanoparticles, J. Eur. Ceram. Soc. 23 (2003) 1697–1704.

[29] A. Krajewski, M. Mazzocchi, P.L. Buldini, A. Ravaglioli, A. Tinti, P. Taddei, C. Fagnano, J. Mol. Struct. 221 (2005) 744–747.

[30] L.M. Rodriguez-Lorenzo, J.N. Hart, K.A. Gross, Influence of fluorine in the synthesis of apatites. Synthesis of solid solutions of hydroxyl-fluorapatite, Biomaterials 24 (2003) 3777–3785.

[31] H.W. Kim, L.H. Li, Y.H. Koh, J.C. Knowles, H.E. Kim, Sol–gel preparation and properties of fluoride-substituted hydroxyapatite powders, J. Am. Ceram. Soc. 87 (2004) 1939–1944.

[32] S.M. Barinov, L.I. Shvorneva, D. Ferro, I.V. Fadeeva, S.V. Tumanov, Solid solution formation at the sintering of hydroxyapatite–fluorapatite ceramics, Sci. Technol. Adv. Mater. 5 (2004) 537–541.

[33] G. Penel, G. Leroy, C. Rey, B. Sombret, J.P. Huvenne, E. Bres, Infrared, Raman microspectrometry study of fluor-fluor-hydroxy and hydroxyapatite powders, J. Mater. Sci.: Mater. Med. 8 (1997) 271–276.

[34] F. Freund, R.M. Knobel, Distribution of fluorine in hydroxyapatite studied by infrared spectroscopy, Dalton Trans., J. Chem. Soc. 6 (1977) 1136–1140.

[35] N. Senamaud, D. Bernache-Assollant, E. Champion, M. Heughebaert, C. Rey, Calcination and sintering of hydroxyfluorapatite powders, Solid State Ionics 101-103 (1997) 1357–1362.

[36] Z. Peng, J. Gong, H. Miao, On the description of indentation size effect in hardness testing for ceramics: analysis of the nanoindentation data, J. Eur. Ceram. Soc. 24 (2004) 2193–2201.